Toward *Pactive* (Passive +Active) Sensing for Improved Identification of Material Properties

ARYA MENON[1] **(Member, IEEE), AND THOMAS M. WELLER**[2] **(Fellow, IEEE)**

[1]Department of Electrical and Computer Engineering, Texas A&M University, College Station, TX 77843, USA

[2]School of Electrical Engineering and Computer Science, Oregon State University, Corvallis, OR 97331, USA

CORRESPONDING AUTHOR: A. MENON (e-mail: aryamenon@tamu.edu)

ABSTRACT Subsurface electromagnetic sensing techniques that can measure material properties of hidden layers are useful for applications such as security screening. A system combining active (radar) and passive (radiometer) sensing into one unit, or a *pactive* sensor, can address drawbacks of extant single mode sensors by reducing measurement ambiguity and resolving features better, thereby leading to improved identification of the hidden layer. This work investigates a technique to noninvasively extract the complex permittivity and thickness of hidden dielectrics using a *pactive* sensor. A proof-of-concept demonstration of an optimization-based inversion technique is used to extract the properties of an unknown, hidden layer in a multi-layered dielectric structure. The technique uses active data to estimate dielectric constant and thickness, and passive data to estimate loss tangent. The experimental setup is selected to represent a simplified single-voxel security scenario consisting of multiple dielectric layers backed by a human phantom layer (heated water). Tests using K-band prototype radar and radiometer systems yielded results with less than 5% error in the extracted dielectric constant, loss tangent and thickness of the unknown layer.

INDEX TERMS Dielectric characterization of embedded layers, security sensing, radar, radiometer.

I. INTRODUCTION

MICROWAVE and millimeter wave security sensors play a significant role in the fight against terrorism and contraband smuggling [1]. The popularity of such sensors stems from the wavelength of operation; millimeter waves are capable of generating high resolution images with modestly-sized antennas, are able to penetrate clothing, and at the same time are non-ionizing in contrast to gamma and X-rays [2]. Depending on the mode of operation, these sensors can be classified into two types – active and passive [1]. An active or radar-based sensor transmits a signal and measures the echo to determine range (distance) and/or reflectivity whereas a passive sensor or radiometer measures the electromagnetic radiation emitted and/or reflected by an object, which is quantified in terms of a noise temperature or an apparent temperature [3]. The capability to measure range enables active sensors to generate 3D images of reflectivity of objects under investigation [4], [5] while images

from passive sensors are typically maps of apparent temperature as a function of location [6]. With enough resolution, both modalities can identify the presence of concealed items. However, specular reflections and clutter from clothing may result in false-alarms [5] thereby decreasing the sensor's effectiveness.

Active and passive modalities provide complementary information and efforts have been made to combine the two into a single system to improve detection rates in security sensors [7], [8]. This idea of combining modalities to improve measurements has been used extensively in remote sensing to study precipitation, sea state, ice cover, etc. [9], [10], [11], [12], [13]. Information obtained from one mode of measurement is often used to interpret that obtained from the other mode [14], [15]. The Consortis project is an example of active-passive sensors in security sensing [8]. It consists of a 340 GHz radar working in conjunction with a dual-band 250/500 GHz radiometer [16], [17], [18]. In addition to

providing complementary information to reduce false alarms, this combined system can overcome disadvantages typically posed by standalone sensors – *e.g.,* active sensors exhibit good dynamic range but offer limited field-of-view at video-rate imaging speeds, while passive imagers have the opposite characteristics with wide field-of-view but poor dynamic range. The project in [16], [17], [18] also created a database of signatures from common contraband. However, to the best of our knowledge, no attempts were made to extract material properties of the contraband.

Passive and active approaches have been used independently for dielectric characterization both in laboratory environments as well as in practical applications. Dielectric characterization using vector network analyzers is carried out by measuring the transmission and/or reflection responses of dielectrics suspended in free space [19], [20] or by inserting samples into waveguide or coaxial line [21]. This technique has been used for characterizing a variety of materials including soil and rock samples for ground penetrating radar applications [22], [23]. The latter requires machining of the dielectric sample and is often undesired. Resonance-based dielectric characterization techniques are inherently narrowband [24] and some resonant techniques such as the dielectric cavity resonator require machining of the sample to fit a certain shape [25]. The coaxial probe method is used to measure the electrical properties of liquids or semi-solids but does not yield good results for solids [20]. Time domain techniques that assume moderate losses have shown the ability to measure complex permittivity profiles of multi-layered dielectrics [26]. However, steps to address ambiguity in extracted layer properties are not addressed. Frequency modulated continuous wave radars have also been used instead of VNAs to measure the dielectric constant using monostatic measurements at different incidence angles [27] and the complex permittivity through monostatic normal incidence [28], [29]. In all these cases, the thickness of the sample is known. In [30], a W band VNA is used to image and characterize explosives placed in front of metallic surfaces and both the thickness and dielectric constant are extracted but not the loss tangent. Theoretical approaches to extract all three parameters of interest – thickness, dielectric constant and loss tangent – of lossy dielectrics using two-sided transmission response [31], one-sided response at two angles of incidence [32], and one-sided cross-polarization response at non-zero angles [33] have also been investigated. However, these techniques do not work for normal incidence, which would be preferred in an application like security sensing. Radiometers are also often used to characterize certain properties of dielectrics in space-borne applications such as measuring the thickness of oil films [34], snow density and soil permittivity [35], etc. In these examples, a single measurement is insufficient to determine the complex permittivity and thickness and therefore, multiple measurements are made at different angles and/or polarizations. If only different polarizations are used, the angle of incidence must be non-zero to observe polarization-dependent differences in the reflection coefficient. With two modes of operation, the *pactive* sensor offers an alternative method to characterize dielectrics that requires data from a single incidence angle and works even when the angle of incidence is zero.

This paper contributes to the literature by presenting a proof-of-concept demonstration of a technique to extract material properties of an embedded dielectric layer, *viz.* thickness, dielectric constant, and loss tangent, using *pactive* data. Consequently, this work attempts to lay the foundation for a technique that can potentially be used for dielectric characterization within a single voxel measurement in security screening applications. Since this work focuses on the technique itself, demonstrations are conducted using independent low-cost prototype K-band (18-26 GHz) radar and radiometric systems as well as a scaled model of a representative multi-layered dielectric target backed by a heated layer to mimic the human body. Despite the focus herein on security sensing, the technique may also be used in conventional laboratory settings especially for millimeter wave/THz material characterization.

The paper is organized as follows: First, Section II describes the system specifications of the prototype radar and radiometer used in this work along with calibration techniques to improve performance. This section is a summary of the authors' previous work and is presented to improve readability of the paper. The dielectric characterization process presented herein involves electromagnetic modeling of the radar and radiometric responses of multi-layered dielectric objects. Section III presents the radar scattering and radiative transfer models for the same. The models are then experimentally verified in Section IV using known materials. Finally, an optimization-based technique to extract the material properties of an unknown embedded dielectric layer within a multi-layered dielectric stack is presented and tested experimentally in Section V. Finally, Section VI considers applicability of the technique to more realistic scenarios.

II. SYSTEM SPECIFICATIONS AND CALIBRATIONS TO IMPROVE PERFORMANCE

Pactive measurements are obtained using independent active and passive sub-systems operating individually in the K band (18 – 26 GHz). The architecture of the radar and radiometer, their performance metrics, and calibration procedures based on our previous work are summarized in this section.

A. THE ACTIVE SYSTEM – FMCW RADAR

The active system is a monostatic frequency modulated continuous wave radar (FMCW) [36]. The block diagram of the radar is shown in Fig. 1 (a). A linear chirp is generated in the 2.25 – 3.25 GHz frequency range, up-converted to the 18-26 GHz band using commercially available frequency multipliers and coupled to a transmitting horn antenna. Echoes from targets are received by a different horn antenna and mixed with the transmitting signal to generate an intermediate frequency (IF) signal whose frequency f_{IF} is
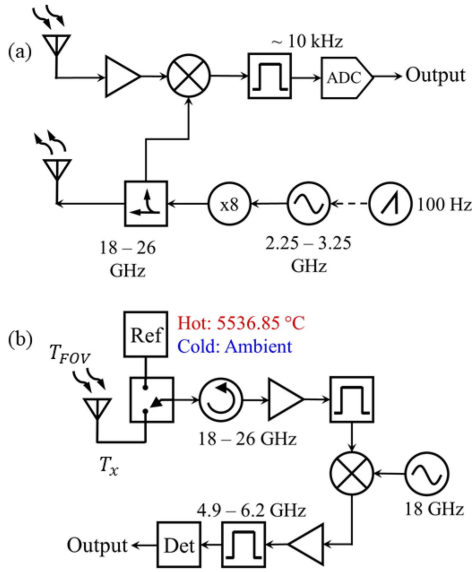
FIGURE 1. (a) Simplified block diagram of the active sensor – an FMCW radar (b) Simplified block diagram of the passive sensor – a total power radiometer. Detailed descriptions are in [36], [39].

directly proportional to the range of the target as $f_{IF} = WT_p$, where $W = 800$ GHz/s is the chirp rate and T_p is the total flight-time of the radar signal to and from the target. The radar's theoretical range resolution is calculated as $\Delta R = v_p/(2\Delta F_{rdr}) = 2$ cm, where v_p is the speed of light in free-space and $\Delta F_{rdr} = 8$ GHz is the bandwidth of the transmitted chirp.

A calibration technique is utilized to improve radar measurements and correct for amplitude and phase distortions introduced into the linear chirp by the RF front-end. The calibration involves a digital correction using a reference IF signal from a highly reflective calibration target at a known distance [37], [38]. The procedure requires the IF signals to be complex - obtained either from an IQ mixer or, for the radar in this work, obtained by calculating the analytic signal using the Hilbert transform. The calibration equation is defined as [38]

$$a_{IF}(t) = \frac{a_{meas}(t)}{a_{cal}(t)} A_{corrc} \tag{1}$$

where, $a_{IF}(t)$ is the calibrated signal, $a_{meas}(t)$ is the complex analytic equivalent of the signal obtained from the scene of interest, $a_{cal}(t)$ is same from the calibration target, and A_{corrc} is a correction factor that is calculated as $A_{corrc} = exp(2\pi j T_{p,cal}(f_0^{rad} + Wt) - \pi j W T_{p,cal}^2)$ [38]. Here, $T_{p,cal}$ is the total flight-time to and from the calibration target, and $f_0^{rad} = 18$ GHz is the minimum frequency of the radar. The frequency content of $a_{IF}(t)$ contains information on the distances to the targets and is extracted through a Fourier transform. The calibrated radar demonstrated a measured range resolution of 2.5 cm [36].

B. THE PASSIVE SYSTEM – TOTAL POWER RADIOMETER

The passive system is a total power radiometer (TPR) operating within 22.9 – 24.2 GHz band [39]. A simplified block diagram of the system is presented in Fig. 1 (b). The radiometer has a gain of 75 dB, front-end isolation of 48 dB, and out-of-band rejection greater than 90 dB. The TPR is continuously calibrated to remove the effects of time-dependent changes in system gain using two calibration noise temperatures – a commercial noise source in the ON state acting as a "hot" reference and the same in the OFF state acting as a "cold" reference. Physical temperatures of the antenna, noise source, and switch are recorded continuously using thermocouples.

### 1) RADIOMETER SYSTEM EQUATION TO CORRECT ERRORS IN THE RF FRONT-END

Accuracy in the measured noise temperature is critical to the *pactive* sensor. Mismatch and insertion loss in the RF-front end lead to errors in the estimated apparent temperature [40]. A radiometer system equation that corrects for mismatch as well as the temperature-dependent noise contributions from insertion loss is derived in [39]. The corrected radiometric temperature T_x measured by the antenna is

$$T_x = T_a' + \beta_H' T_H' + \beta_C' T_C' + \Delta T_i' \tag{2}$$

where, T_a' includes the physical temperature of the antenna T_p^p and scaled versions of the physical temperatures of all components before the isolator; T_H' and T_C' are the modified hot and cold calibration temperatures to include system losses; β_H' and β_C' are calculated using measured powers delivered from the antenna, cold reference, hot reference and mismatch factors; and $\Delta T_i'$ is a correction factor. These terms are fully defined in [39], where (2) is shown to be an accurate model of all losses in the radiometer front-end through experiments. T_x is converted to apparent temperature by correcting for antenna effects, as discussed below. Note that all physical temperatures in this work are denoted with the superscript p.

2) A CALIBRATION TECHNIQUE TO MEASURE AND CORRECT FOR BACKGROUND NOISE TEMPERATURE

In addition to measuring electromagnetic radiation from its field-of-view (FOV), the antenna also captures portions of the apparent temperature of the background from the side-lobes (T_{SL}) and that reflected off the target (T_{refl}) as shown in Fig. 2 (a). A calibration technique to measure and correct for T_{SL} and T_{refl} is presented in [41]. The technique, summarized in Fig. 2 (b), consists of three steps: measuring a pyramidal absorber at a known temperature $T_{py.ab}^p$, measuring a metal plate, and finally applying corrections to measurements. In this work, as in [41], the radiometer results are presented in terms of apparent noise temperature in the field of view T_{FOV}. The measured background noise component T_{refl} is used in the radiometric model to simulate the expected T_{FOV}
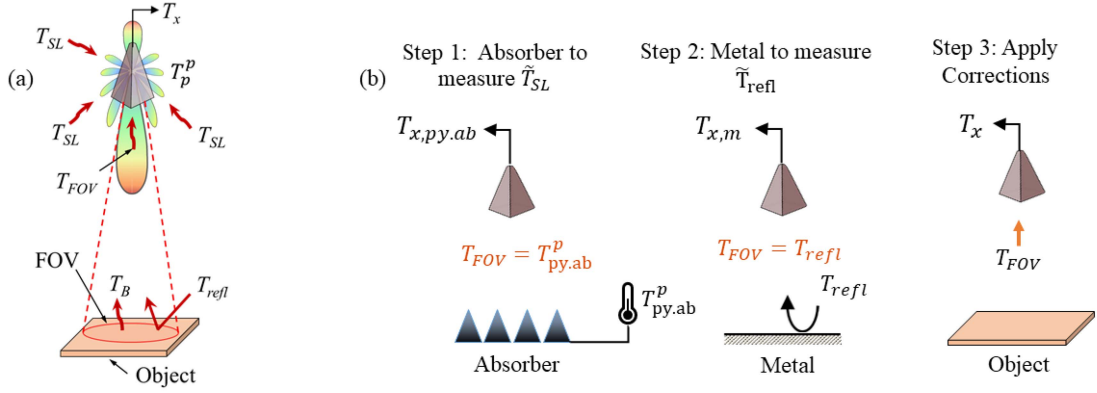
FIGURE 2. (a) Sources of background noise during radiometric measurements and (b) steps in the background calibration technique described in Section II-B2 [41].

using

$$T_{FOV} = T_B + \Gamma \cdot T_{refl} \quad (3)$$

where, Γ and T_B are the effective reflectivity and brightness temperature of the object, respectively. Measured T_{SL} is used to extract measured $\widetilde{T}_{FOV}$ from measured antenna temperature T_x (see (2)) using

$$\widetilde{T}_{FOV} = \frac{1}{\xi \eta_{FOV}} \left(T_x - \xi(1-\eta_{FOV})T_{SL} - (1-\xi)T_p^p \right) \quad (4)$$

where, ξ is the radiation efficiency of the antenna, η_{FOV} is the effective beam efficiency and T_p^p is the physical temperature of the antenna. In this work, $\xi = 93\%$ and $\eta_{FOV} = 40\%$. This calibration approach results in accurate measurements in noisy indoor environments as demonstrated in [41]. The feasibility of such a calibration scheme for non-laboratory settings is also justified in [41].

Hence, the Hilbert transform-based radar calibration and radiometric corrections using the radiometer system equation and the background correction scheme are essential towards correcting some of the errors in the measurement. The corrected results improve the ability to model the multi-layered dielectric targets as discussed in the next section.

III. MODELING OF MULTI-LAYERED DIELECTRIC TARGETS

Radar and radiometric models to calculate the response of the sensors are presented in this section. The targets are modeled as stratified dielectrics with N layers each with thickness d_i, complex relative permittivity $\varepsilon_i = \varepsilon'_i - j\varepsilon''_i$, and propagation constant k_i as shown in Fig. 3 (a). The complex permittivity is related to loss tangent as $tan\delta_i = \varepsilon''_i/\varepsilon'_i$. The dielectric stack is placed at a distance of R_0 from the *pactive* sensor. Modeling both the radar and radiometric responses from such targets requires calculation of the effective reflection coefficient ρ_e of the dielectric stack. The following assumptions are made (i) the target is in the far-field of the antenna, (ii) the target's lateral dimensions extend beyond the FOV of the antenna, and (iii) the first layer (air) and last (N^{th}) layer are semi-infinite.
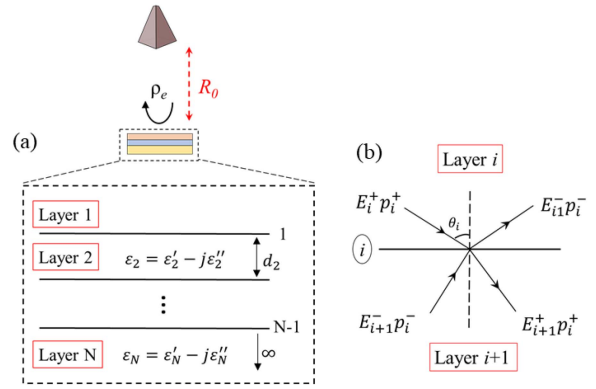
FIGURE 3. (a) Targets modeled as a multi-layer dielectric with N layers. The dielectrics are placed at a distance of R0 from the sensor. (b) Reflected and transmitted fields at interface i between layers i and i+1.

Electric fields at frequency f in each layer are modeled as shown Fig. 3 (b) based on the mathematical treatment in [42]. Electric fields E_i^+ and E_i^- are defined in each layer i. Propagator functions $p_i^{\pm}$ are defined at each interface i and calculated using

$$p_i^{\pm} = e^{\pm jk_i d_i cos\theta_i} p_{i-1}^{\pm} \quad (5)$$

$$p_1^{\pm} = 1 \quad (6)$$

$$p_i^+ = \left(p_i^-\right)^{-1} \quad (7)$$

where, θ_i is the angle of propagation in each layer and is calculated using Snell's Law. The net fields on either side of interface i depend on the electric fields and propagator functions as shown in Fig. 3 (b). The refractive index is $n_i = \sqrt{\varepsilon_i^*}$, where the conjugate of complex permittivity is used to define refractive index because [42] follows the $e^{-i\omega t}$ convention. For normal incidence, $\theta_i = 0$. Solving for boundary conditions, the electric field in any layer i is calculated from that in layer $i+1$ as

$$\begin{bmatrix} E_i^+ \\ E_i^- \end{bmatrix} = \begin{bmatrix} (p_i^+)^2 & 1 \\ (p_i^+)^2 & -1 \end{bmatrix}^{-1} \begin{bmatrix} (p_i^+)^2 E_{i+1}^+ + E_{i+1}^- \\ \frac{n_{i+1}cos\theta_{i+1}}{n_i cos\theta_i}\left((p_i^+)^2 E_{i+1}^+ - E_{i+1}^-\right) \end{bmatrix} \quad (8)$$

for horizontal (perpendicular/ TE) polarized and

$$\begin{bmatrix} E_i^+ \\ E_i^- \end{bmatrix} = \begin{bmatrix} (p_i^+)^2 & 1 \\ (p_i^+)^2 & -1 \end{bmatrix}^{-1} \begin{bmatrix} \frac{cos\theta_{i+1}}{cos\theta_i}\left((p_i^+)^2 E_{i+1}^+ + E_{i+1}^-\right) \\ \frac{n_{i+1}}{n_i}\left((p_i^+)^2 E_{i+1}^+ - E_{i+1}^-\right) \end{bmatrix} \quad (9)$$

for vertical (parallel/TM) polarization.

Assuming that $E_N^+ = 1$ and $E_N^- = 0$ (since the Nth layer is semi-infinite), (8) or (9) is solved iteratively to calculate the electric fields in each layer. Finally, the fields are renormalized with E_1^+ to make the field incident on the composite structure equal to 1. The effective reflection coefficient at a frequency f is hence calculated as

$$\rho_e = \left(\frac{E_1^-}{E_1^+}\right)^* \quad (10)$$

The effective reflection coefficient ρ_e may also be calculated using other approaches such as the wave matrix method in [43] or transmission line method [3]. In (10), the complex conjugate ensures that the phase of the reflection coefficient changes in accordance with the $e^{j\omega t}$ convention, which is preferred in this work. The effective reflectivity Γ of the multi-layer structure is defined as

$$\Gamma = |\rho_e|^2 \quad (11)$$

The effective reflectivity is related to the effective emissivity as described in [3] and is used instead of emissivity in this work.

A. MODELING THE RADAR RESPONSE
The radar response P_{rdr} is computed using MATLAB as [44]

$$P_{rdr}(\zeta) = \mathcal{F}^{-1}\left(\rho_e(f)e^{-2jk_1(f)R_0}\right)$$
$$\text{for } f_0^{rad} \leq f \leq (f_0^{rad} + \Delta F_{rdr}) \quad (12)$$

where, $\mathcal{F}^{-1}$ denotes the inverse Fourier transform and ζ is time, i.e., the inverse Fourier transform variable, f_0^{rad} is the start frequency of the radar and ΔF_{rdr} is the radar bandwidth. ζ is converted to range R using the transformation $R = v_p\zeta/2$, where v_p is the speed of light in free space. The amplitude of the radar range profile is plotted in normalized form as $|P_{rdr}(\zeta)|^2 / \max |P_{rdr}(\zeta)|^2$.

B. MODELING THE RADIOMETER RESPONSE
Wilheit's approach to radiative transfer for non-isothermal layers is used to calculate the radiometric response [42]. The apparent temperature of a dielectric stack at any frequency f is

$$T_{AP}(f) = \sum_{i=1}^{n} S_i T_i^p + \Gamma.T_{refl} \quad (13)$$

where, T_i^p is the physical temperature of the ith layer, T_{refl} is the background temperature reflected off the multi-layer dielectric as described in Section II-B2, and S_i is the fraction

of radiation incident on the ith interface which would be absorbed by the ith layer, and is calculated as

$$S_i = \frac{1}{cos\theta_i}\Bigg[Re(n_i cos\theta_i)|E_i^+|^2\left(|p_{i-1}^+|^2 - |p_i^+|^2\right)$$
$$+ Re(n_i cos\theta_i)|E_i^-|^2\left(\left|\frac{1}{p_i^+}\right|^2 - \left|\frac{1}{p_{i-1}^+}\right|^2\right)$$
$$+ 2Imag(n_i cos\theta_i) * Imag\left(E_i^+(E_i^-)^*\left(\frac{p_{i-1}^+}{(p_{i-1}^+)^*} - \frac{p_i^+}{(p_i^+)^*}\right)\right)\Bigg] \quad (14)$$

The average of the apparent temperature over the frequency band of the radiometer is used for the model since the radiometer in this work is relatively wide-band and the reflectivity may change significantly within the band. Assuming that the apparent temperature is not a function of angle within the FOV of the antenna, the simulated temperature in the field-of-view of the radiometer is

$$T_{FOV} = \frac{1}{M}\sum_{i=1}^{M} T_{AP}(f_i)\Big|_{f_0^{rdmtr}}^{f_0^{rdmtr}+\Delta F_{radm}} \quad (15)$$

where, f_0^{rdmtr} is the start frequency of analysis, M is the number of frequency points in the analysis and ΔF_{radm} is the bandwidth of the radiometer. In security sensing, the physical temperature of a concealed object can be assumed to be equal to human body temperature [18] simplifying (13) to (3), which is the isothermal case. However, the non-isothermal model in (15) in the remainder of this paper as it is the general case and applicable to the objects measured in this work.

The radar and radiometric models for planar, multi-layered dielectrics presented above are tested experimentally in the following section using the K-band *pactive* sensor and multilayered targets. The models are frequency scalable and applicable to any number of layers. The models assume that the first (air) and last (skin/skin-mimicking) layers are semi-infinite. This assumption is valid at high frequencies where the skin depth of the radiation in the human body is a few millimeters.

IV. EXPERIMENTAL SETUP AND MEASUREMENTS
The models in Section III are validated using known objects consisting of different dielectric layers stacked on top of warm water, which represents a simplified human body phantom. The depth of water (1.56 cm) is chosen to ensure that its HDPE container does not contribute to the radar/radiometric responses. Hence, the water is assumed to be a semi-infinite layer while modeling. The targets are placed at approximately $R_0 = 2$ m from the measurement system as shown in Fig. 5 (a), which is in the far-field of the horn antennas used in this work. Four different configurations of dielectrics are studied as shown in Fig. 4 – configuration #1, 2, 3 and 4 consisting of N = 5, 5, 6, 6 layers, respectively. The thickness, dielectric constant and loss tangent of each dielectric

TABLE 1. Materials used in experimental setup.

Material	Thickness (mm)	Dielectric Constant	Loss tangent
AD450 [45]	4.065	4.5	0.004
LDPE	1.524	2.2	0.0003
ABS [46]	10	2.4	0.0075
Styrofoam	58	1	0
Air	16.4	1	0
Water	15.6	$\varepsilon_w(f, T_w^p)$ [48]	$tan\delta(f, T_w^p)$[48]
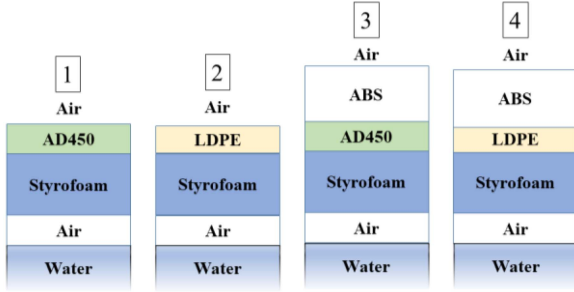
FIGURE 4. Dielectric stack configurations used to test and correct electromagnetic models. The properties of the materials are in Table 1.

material are listed in Table 1 [45], [46]. These dielectrics were chosen as their electrical properties are similar to those of representative concealed items, e.g., the dielectric constant of explosive material typically falls between 2.7-3.2 with loss tangents of the order of 0.001 [47]. The cross-sectional area of all materials is 30 cm × 30 cm, which is larger than the area subtended by the antenna's main beam. The electrical properties of water are calculated at the desired frequency and temperature using the model in [48].

Radar and radiometric measurements are made for each configuration separately. Water is heated to approximately 328 K and allowed to cool in the HDPE container. As the water cools, radar/radiometric measurements are made individually while the temperature of the water T_w^p is recorded using a thermocouple. All other layers are assumed to be at room temperature (295.15 K). For radiometric measurements, the background calibration from Section II-B2 is performed every 15 minutes to obtain a calibration set. Each calibration set consists of radiometric temperatures obtained over 5 minutes each for the absorber and metal calibration targets. The average between the calibration coefficients bounding the 15 minutes data acquisition is used for the correction [41]. This calibration scheme was incorporated to account for time varying noise temperature fluctuations within the laboratory. For the radar, calibration with a metal plate (Section II-A1) placed at $R_0 = 2$ m every 1.5 hours is sufficient.

Initial data from these experiments suggest that while the calibration techniques presented in Section II improve measurement accuracy of single-layered targets, they do not account for measurement artifacts observed with multi-layered dielectric targets. These artifacts are believed to be the result of unwanted harmonics in the radar response and non-ideal filtering in the radiometer response. Hence, correction factors are introduced to the models to improve the fit (see Figs. 5–7) between the modeled response and the measurements. A system specific correction factor of 1 GHz frequency shift in the radar model is introduced so that the modeled radar range response fits the measurements better over all the four dielectric configurations as shown in Fig. 6. The radar response model described by (12) is corrected to

$$P_{rdr}(\zeta) = \mathcal{F}^{-1}\left(\rho_e(f)e^{-2jk_1(f)R_0}\right),$$
$$f' \leq f \leq \left(f' + \Delta F_{rdr}\right) \qquad (16)$$

where, $f' = f_0^{rad} + f_{corr}^{rad}$, $f_{corr}^{rad} = 1$ GHz is the radar correction factor, $f_0^{rad} = 18$ GHz and $\Delta F_{rdr} = 8$ GHz. The term f_{corr}^{rad} is a first-order correction factor that accounts for unwanted harmonic-induced chirps in the radar's passband. Single tone measurements in the radar's passband using a spectrum analyzer (see the Appendix) show the presence of harmonics that sweep during the radar's operation. As discussed in Section II, the prototype FMCW radar is built using commercially available off-the-shelf components in which a low frequency chirp is passed through a series of frequency multipliers to get the signal in the desired band. However, the harmonics generated during multiplication are insufficiently filtered in the system. While the calibration has been experimentally proven to work in the presence of multiple metallic targets in our previous work [36], it appears that calibration efficacy decreases due to the presence of harmonics when the targets are not highly reflective. The correction factor f_{corr}^{rad} is expected to be less significant in a future iteration of the radar where the chirp will either be directly generated in the K-band or better filters will be used in the multiplier chain.

The measured and simulated radar range profiles for the four dielectric configurations are shown in Fig. 6. Apart from a slight shift in range for configurations #3 and #4, the measured and modeled range profiles match well. Note that normalized amplitudes are plotted in the radar range profiles in this work since the unnormalized amplitudes do not match. In addition to the radar range profile, the normalized calibrated radar signal $|a_{IF}(t)|$, as defined in (1), for dielectric configuration #1 is plotted in Fig. 7 (a) along with the magnitude of the modeled effective reflection coefficient $|\rho_e(f)|$. Similarity between the two plots suggests a direct relationship between $|a_{IF}(t)|$ and $|\rho_e(f)|$. This relationship follows from the Fourier transform in (16) as well as the Fourier relationship between the output of the mixer and the radar range profile.

The radiometer correction factor accounts for system-specific non-idealities such as imperfect filtering. The
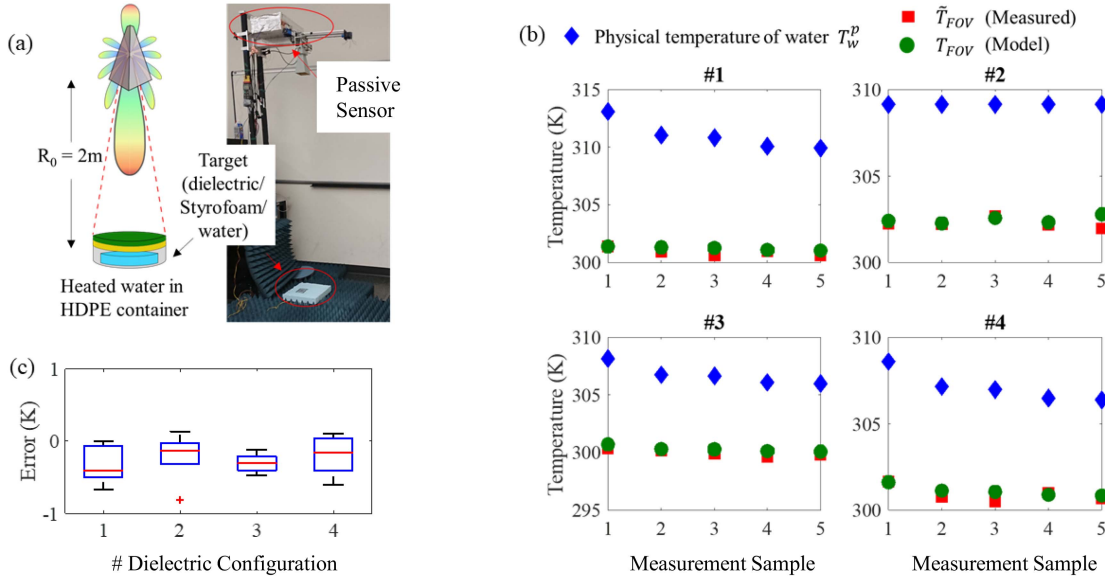
FIGURE 5. (a) Measurement setup when the passive sensor is connected (b) Measured and modeled response of the radiometer for the four dielectric configurations in Fig. 4. Five measurement samples are recorded. (c) Error in the radiometric measurement.
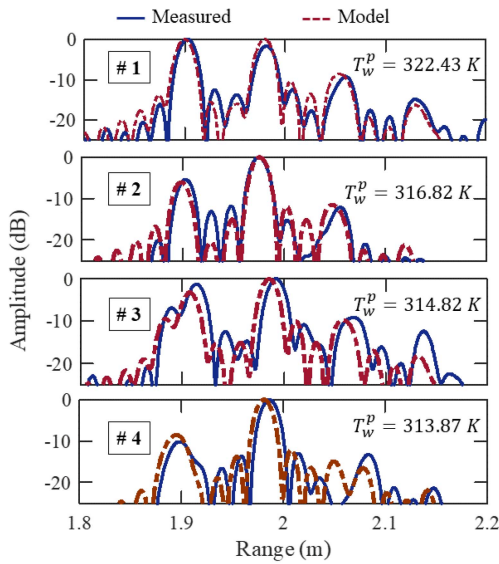

FIGURE 6. Measured and modeled radar range response for the four dielectric stack configurations in Fig. 4. The temperature of water T_w^p is inset.

radiometer model in (15) is modified to

$$T_{FOV} = \frac{1}{M} \sum_{i=1}^{M} T_{AP}(f_i)\Big|_{f_0^{rdmtr} - f_{corr}^{rdmtr}}^{f_0^{rdmtr} + \Delta F_{radm}} \qquad (17)$$

where, $f_{corr}^{rdmtr} = 0.2$ GHz is the radiometric correction factor which is modeled as an increase in the bandwidth by 200 MHz, $f_0^{rdmtr} = 22.9$ GHz, $\Delta F_{radm} = 1.3$GHz is the radiometer's bandwidth, and the equation is evaluated at M frequency points.

Five radiometric measurements (samples) of $\widetilde{T}_{FOV}$ at different T_w^p for each of the four dielectric configurations along with the corresponding modeled T_{FOV} are shown in
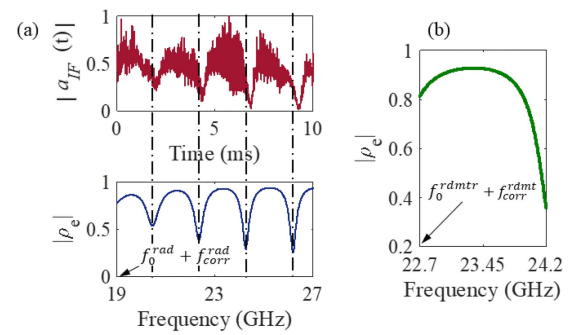

FIGURE 7. Plots corresponding to configuration #1: (a) Measured normalized radar signal $|a_{IF}(t)|$ vs modeled effective reflection coefficient $|\rho_e|$ in the radar band (b) Modeled effective reflection coefficient $|\rho_e|$ in the radiometer band.

Fig. 5 (b). The error, $\widetilde{T}_{FOV} - T_{FOV}$, is plotted in Fig. 5 (c) and shows that the model is accurate with an average error less than 0.5 K across the four configurations.

To summarize, the models in Section III are modified to account for errors that are not corrected by the calibration techniques. The models are experimentally validated using four multi-layered dielectric stacks and both the radar and radiometric results show good match between model and measurements. Further, the reflection coefficient shows a significant variation across frequency within both the radar and radiometer bandwidth (Fig. 7 (b)) demonstrating the need for modeling the frequency response across the band.

V. EXTRACTION OF MATERIAL PROPERTIES FROM PACTIVE MEASUREMENTS

A technique to non-invasively extract the thickness, dielectric constant, and loss tangent of a dielectric using the *pactive* measurements is presented in this section. The dielectric configuration in Fig. 8 (a) is used for the experimental
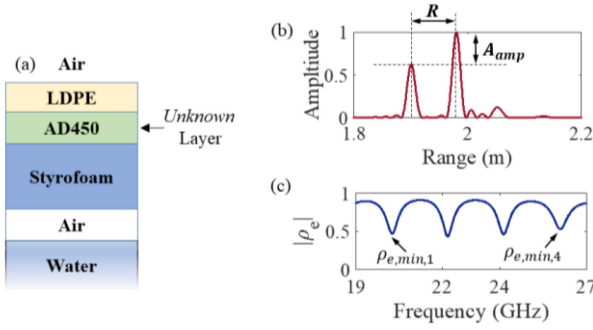
FIGURE 8. (a) Dielectric configuration used for extraction study. AD450 layer is unknown. (b) radar range response to show parameters R and A_{amp} in the objective functions (c) magnitude of effective reflection coefficient to show parameter $\rho_{e,min,i}$ in the objective functions.

FIGURE 9. Objective functions for extraction process. Plots in the left column are the radiometer-based objective function while those in the right column are the radar-based objective function. Plots are for the configuration in Fig. 8: (a) as a function of thickness d when permittivity ε_r and loss tangent *tanδ* are constant as listed (b) as a function of ε_r when d and *tanδ* are constant, (c) as a function of *tanδ* when ε_r and d are constant.

demonstration where the thickness d, dielectric constant ε_r, and loss tangent *tanδ* of the AD450 layer are unknown. The rest of the layers are known, and their properties are described in Table 1. The physical temperature of the water T_w^p is recorded during measurement and all other layers are assumed to be at room temperature 295.15 K. The extraction process is set up as an optimization problem consisting of four objective functions – one of which describes the radiometer response and the other three describe the radar response. The objective function ΔT_{FOV} calculates the square of the error in the radiometer response as

$$\Delta T_{FOV} = \left(T_{FOV}^{meas}\left(T_w^p\right) - T_{FOV}^{sim}\left(d, \varepsilon_r, tan\delta, T_w^p\right) \right)^2 \quad (18)$$

where, $T_{FOV}^{meas}(T_w^p)$ is the measured apparent temperature in the field-of-view at water temperature T_w^p and $T_{FOV}^{sim}(d, \varepsilon_r, tan\delta, T_w^p)$ is the corresponding modeled value from (17). The unit of ΔT_{FOV} is K^2. Equations (19)–(20) describe the three radar-based functions. The first radar-based objective function is
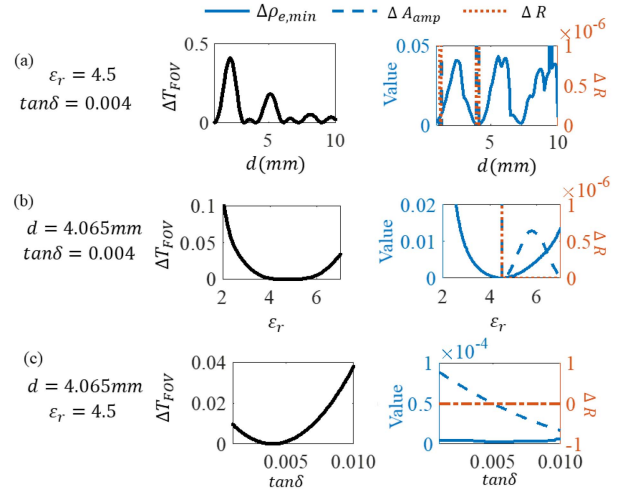
$$\Delta \rho_{e,min} = \frac{1}{m} \sum_{i=1}^{m} \left(\rho_{e,min,i}^{meas} - \rho_{e,min,i}^{sim}\left(d, \varepsilon_r, tan\delta, T_w^p\right) \right)^2 \quad (19)$$

where, the unit of $\Delta \rho_{e,min}$ is Hz^2. As observed in Section IV, a one-to-one mapping exists between $|a_{IF}(t)|$ and $|\rho_e(f)|$. Hence, $|a_{IF}(t)|$ is mapped to $|\rho_e^{meas}(f)| = |a_{IF}(t \to f)|$ after a change of variable from t to f. In (19) $\rho_{e,min,i}^{meas}$ represents the location of the ith minimum in Hz (see Fig. 8(c)), $\rho_{e,min,i}^{sim}(d, \varepsilon_r, tan\delta)$ are the corresponding modeled values, and m represents the total number of minima. If at any point during the optimization process, the number of minima in $\rho_{e,min,i}^{sim}$ is not equal to the number of minima in $\rho_{e,min,i}^{meas}$, then $\Delta \rho_{e,min}$ is set a large value such as 2×10^4.

The second radar-based objective function is

$$\Delta A_{amp} = \left(A_{amp}^{meas} - A_{amp}^{sim}\left(d, \varepsilon_r, tan\delta, T_w^p\right) \right)^2 \quad (20)$$

where, A_{amp}^{meas} is the difference in the normalized amplitude of the peaks in the radar range response (Fig. 8 (b)) and $A_{amp}^{sim}(d, \varepsilon_r, tan\delta)$ is the corresponding difference in the model.

If the number of significant peaks in the radar range profile during optimization is not equal to that in the measurement, ΔR and ΔA_{amp} are set to a large value 2×10^4 to prompt the optimizer to ignore the selected combination of $(d, \varepsilon_r, tan\delta)$. The decision on what makes a peak 'significant' is based on the amplitude of the two peaks in the measured range response. From Fig. 8 (b), the first two peaks have normalized amplitudes of 0.6216 and 1, respectively. Hence, for this analysis, any peak in the radar range response is considered significant if it has an amplitude greater than 0.6.

Variation of the four objective functions with any one material parameter when the other two are constant for the dielectric stack under consideration is shown in Fig. 9. All four objective functions are strongly dependent on d and ε_r as shown in Fig. 9 (a) and (b). A local minimum occurs for the correct values of the unknown AD450 layer's properties, i.e., $d = 4.065$ mm and $\varepsilon_r = 4.5$. The presence of multiple local minima in Fig. 9 (a) presents a challenge to the extraction process – the optimization technique must be robust enough to not converge at a local minimum. Additionally, from Fig. 9 (c), the radar objective functions are seen to be independent of *tanδ*. If all four functions are simultaneously optimized for the three unknowns $(d, \varepsilon_r, tan\delta)$, the optimizer may not converge to the correct answer since three of the objective functions are independent of one variable. Taking this to account, two-step optimization is proposed:

1) MULTI-OBJECTIVE OPTIMIZATION

The three radar objective functions are optimized simultaneously using the Pareto-front approach to calculate a set of thickness $\{\tilde{d}\}$ and dielectric constant values $\{\tilde{\varepsilon}_r\}$:

Minimize $\Delta\rho_{e,min}, \quad \Delta R, \quad \Delta A_{amp}$

Subject to $\varepsilon_{min} \leq \varepsilon_r \leq \varepsilon_{max}$ and $d_{min} \leq d \leq d_{max}$

TABLE 2. Inputs to optimization algorithm.

	Ideal	Measured (Coarse)	Measured (Fine)
T_{FOV}^{meas} (K)	301.7	301.71	301.91
T_w^p (K) (Radiometer)	309.87	309.87	314.93
T_{refl} (K)	298.22	298.22	297.65
$\rho_{e,min,i}^{meas}$ (GHz)	20.2531 22.1846 24.1274 26.0926	20.3107 22.2086 24.1738 26.1934	NA
R^{meas} (m)	0.079	0.078	NA
A_{amp}^{meas}	0.3784	0.3362	NA
T_w^p (K) (Radar)	320.7	320.7	NA

FIGURE 10. Extraction of material properties for ideal inputs when (a) thickness d of the layer is known (b) none of the properties of the layer are known.

where, ε_{min} and ε_{max} are minimum and maximum allowed dielectric constant values, respectively, and d_{min} and d_{max} are the minimum and maximum allowed thickness, respectively. Since the radar functions are independent of $tan\delta$, an arbitrary value can be used. In this work, the optimization is carried out using multi-objective particle swarm optimization [49].

2) CALCULATE TANδ

Use $\{\widetilde{d}\}$ and $\{\widetilde{\varepsilon_r}\}$ from Step 1 and find the corresponding loss tangent that minimizes ΔT_{FOV} over a range of allowed values defined by $(tan\delta_{min}, tan\delta_{max})$. The result is a set of possible loss tangent values $\{tan\widetilde{\delta}\}$.

A. EXTRACTION OF MATERIAL PROPERTIES WITH IDEAL (SIMULATED) DATA
1) WHEN THICKNESS OF THE LAYER IS KNOWN

The process described above is tested for ideal data generated using the MATLAB models. In the first part of the study, the thickness of the AD450 layer $d = 4.065$ mm is assumed to be known. Inputs to the algorithm are listed in Table 2. The multi-objective particle swarm optimization algorithm is initiated with 50 particles and run for 100 iterations to arrive at $\{\widetilde{\varepsilon_r}\}$, following which step 2 calculates $\{tan\widetilde{\delta}\}$ completing the extraction process. The following bounds are applied during optimization: $d_{min} = 1$ mm, $d_{max} = 10$ mm, $\varepsilon_{min} = 2$, $\varepsilon_{max} = 7$, $tan\delta_{min} = 0.001$, $tan\delta_{max} = 0.1$. The results are shown in Fig. 10 (a) wherein the possible solutions are displayed as a histogram. Since the thickness is known, a single line is displayed in the histogram for $\{\widetilde{d}\}$. Most of the entries for $\{\widetilde{\varepsilon_r}\}$ and $\{tan\widetilde{\delta}\}$ converge to the correct values of $\varepsilon_r = 4.5$ and $tan\delta = 0.004$ demonstrating that the proposed technique works when one variable is known.

2) WHEN ALL PARAMETERS OF THE SAMPLE ARE UNKNOWN

When all parameters are unknown, the optimizer converges to values within the vicinity of the actual value as shown in
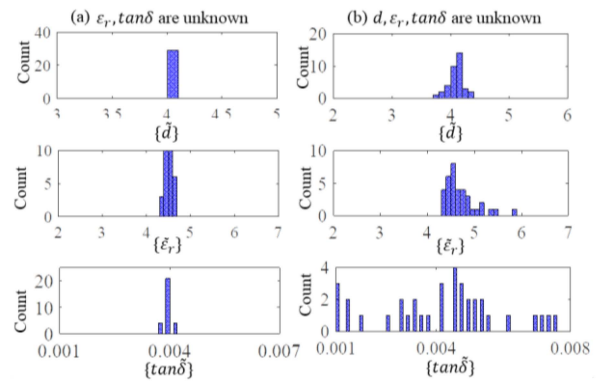
Fig. 10 (b). The most likely values obtained from Fig. 10 (b) are $\widetilde{d} = 4.102$ mm, $\widetilde{\varepsilon_r} = 4.48$, and $tan\widetilde{\delta} = 0.0045$. This corresponds to an error of 0.9%, 0.4% and 12.5% in thickness, dielectric constant and loss tangent, respectively. The initial error in $\{\widetilde{d}\}$ and $\{\widetilde{\varepsilon_r}\}$ results in a larger error in $tan\widetilde{\delta}$, which would be unacceptable in practice. The accuracy of the extracted properties is improved with an additional data point as discussed below with measured data. At the same time, knowing the approximate range may sometimes be sufficient for certain applications.

3) EXTRACTION OF MATERIAL PROPERTIES WITH MEASURED DATA

In this sub-section, measured passive and active data is used for the extraction of dielectric properties. The experimental process for data acquisition is described in Section IV and the dielectric configuration with the unknown AD450 layer is considered once again. Comparison between measured and modeled data in Fig. 11 shows the presence of measurement errors. The minima in the radar data in Fig. 11 (a) do not line up exactly, the measured first peak in the radar range profile (Fig. 11 (b)) is higher in magnitude. Further, the radiometric measurements in Fig. 11 (c) do not match the model for some of the higher water temperatures. Modification of the extraction process is needed to obtain good results despite these errors since data from a real-world scenario could be noisy.

A two-step optimization approach consisting of coarse and fine optimizations is introduced to improve accuracy. The process described in Section V-A is used to find coarse range of possible values $\{\widetilde{d_1}\}$, $\{\widetilde{\varepsilon}_{r,1}\}$ and $\{tan\widetilde{\delta_1}\}$ followed by a fine optimization using an additional radiometric data point $T_{FOV}^{meas,2}$. This process is described schematically in Fig. 12 (a). The inputs to the optimizer for the dielectric configuration under consideration for both the coarse and fine optimization steps are listed in Table 2. Fig. 12 (b) shows the solution set obtained using the coarse optimization. The solution space for coarse optimization is defined by the bounds: $d_{min} = 1$ mm, $d_{max} = 10$ mm, $\varepsilon_{min} = 2$, $\varepsilon_{max} = 7$, $tan\delta_{min} =$
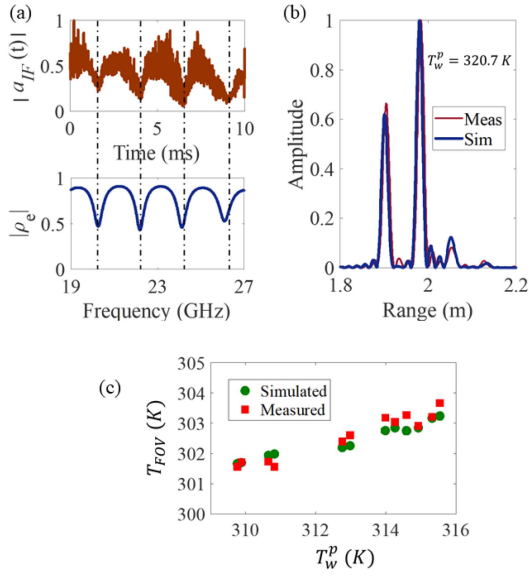
FIGURE 11. Measured vs modeled (simulated) results for dielectric configuration in Fig. 8: (a) comparison between normalized measured radar signal $|a_{IF}(t)|$ and modeled reflection coefficient $|\rho_e|$. (b) radar range profile: measured vs modeled (c) measured and simulated radiometric temperatures T_{FOV} for different water temperatures T_w^p.
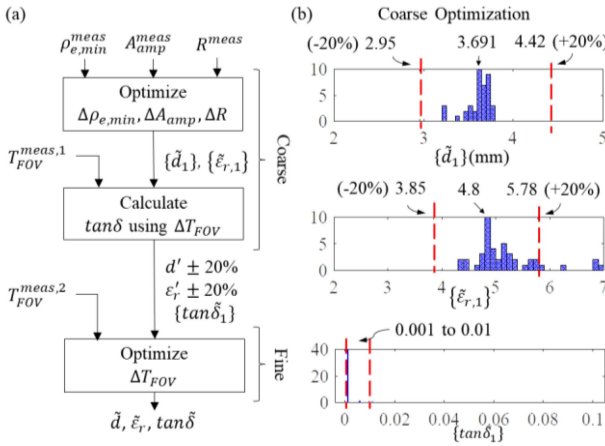
FIGURE 12. (a) Process for extracting thickness $\tilde{d}$, dielectric constant $\tilde{\varepsilon}_r$ and loss tangent $tan\tilde{\delta}$ (b) Results of coarse optimization. The indicated range is used for the fine optimization.

0.001, $tan\delta_{max} = 0.1$. A $\pm 20\%$ range around the most probable values (d', ε_r') is selected as the input range for fine optimization. For loss tangent, a 10x range is used instead of $\pm 20\%$. This reduces the optimization space to $d_{min} = 2.95$ mm, $d_{max} = 4.42$ mm, $\varepsilon_{min} = 3.85$, $\varepsilon_{max} = 5.78$, $tan\delta_{min} = 0.001$, $tan\delta_{max} = 0.01$. The updated optimization range along with a radiometric measurement $T_{FOV}^{meas,2}$ at a different water temperature are fed into a second particle swarm algorithm to optimize the function ΔT_{FOV}. Since only one objective function is optimized, the output of the optimizer is a single point $(\tilde{d}, \tilde{\varepsilon}_r, tan\tilde{\delta})$ in the three dimensional optimization space. The result after fine optimization is shown in Table 3 where the error percentage is less than 5% for all three extracted properties. In practice, instead of measurement at different temperature, measurement at a

TABLE 3. Extracted material properties and error.

Material Property	Estimate	Actual	Error
Thickness (mm)	4.14	4.065	1.8 %
Dielectric Constant	4.71	4.5	4.67 %
Loss Tangent	0.0041	0.004	2.5 %

TABLE 4. Materials used for analysis in Fig. 13.

Material	Thickness (mm)	Dielectric Constant	Loss tangent
Polyester Clothing @ 2.6 GHz [51]	1	1.9	0.0045
MUT #1	56	2.5	0.014
MUT #2	45	3.9	0.0008
Skin @ ~ 25 GHz [50]	NA	19	1.053

different frequency may be used. Hence, the presented technique offers a method to extract the electrical properties and thickness of an embedded layer within a dielectric stack.

VI. APPLICABILITY TO OTHER SCENARIOS

Although different material configurations can lead to different objective function behavior, the general optimization process is still applicable. In the previous section, the extraction process is validated for a dielectric configuration consisting of two thin, relatively low-loss layers separated from warm water by a spacer layer. To address broader applicability of the technique, a security scenario consisting of an unknown material MUT #1 concealed between polyester clothing and skin as shown in Fig. 13 (a) is studied in this section. MUT #1 is assumed to be thick and lossy with dielectric constant, loss tangent, and thickness of 2.5, 0.014, and 56 mm, respectively. The properties of the remaining layers are listed in Table 4 [50], [51]. The permittivity of polyester in the K-band is assumed to be the same as the value reported in [51] at 2.6 GHz. The four objective functions for this configuration are plotted in Fig. 13 (b)-(d). Since the unknown material is thick and lossy, the radar objective function A_{amp}^{meas} now depends on $tan\delta$ (Fig. 13(d)) unlike the one presented previously. In this analysis, the cutoff for significant peaks is set to 0.2. The behavior of the remaining objective functions is similar to the ones in the previous section. It may be argued that A_{amp}^{meas} can be used to find $tan\delta$ once (d, ε_r) are obtained using the other two radar-based objective functions. However, other solutions that fit the radar model exist. The radiometer is thus essential towards removing measurement ambiguity. Overall, the extraction technique presented in this work can still be applied with minor modifications such as removing ΔA_{amp} from the initial coarse optimization step since it strongly depends on $tan\delta$. Although the objective functions may
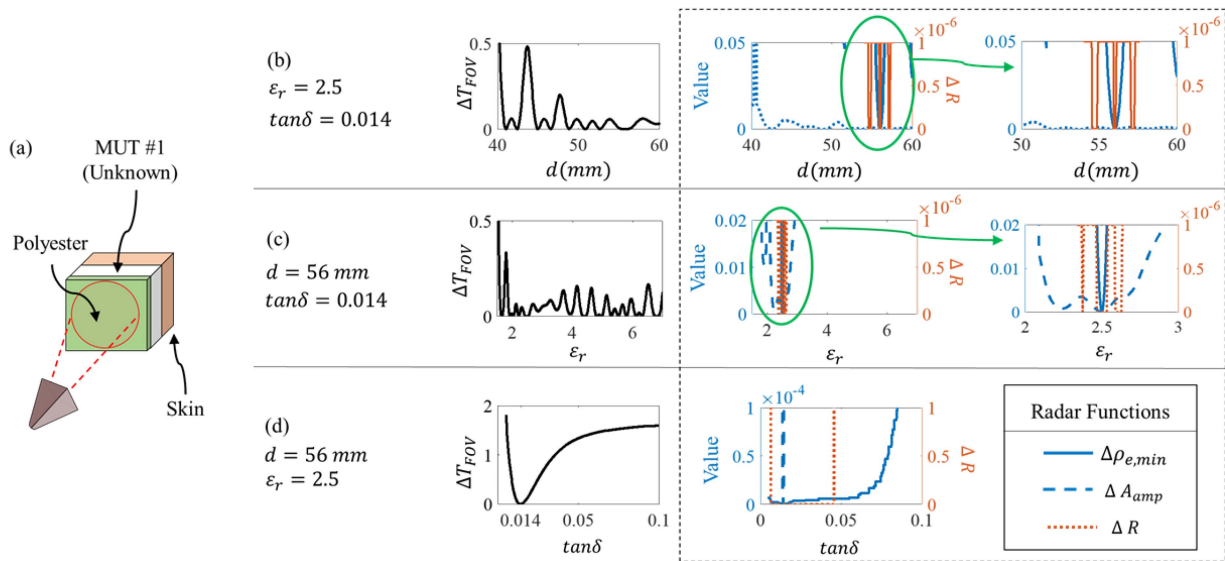
FIGURE 13. (a) Dielectric stack of interest. MUT #1 is unknown (b) objective functions as a function of thickness d when permittivity ε_r and loss tangent $tan\delta$ are constant and as listed, (b) as a function of ε_r when d and $tan\delta$ are constant, (c) as a function of $tan\delta$ when ε_r and d are constant.

not necessarily behave the same way for other dielectric configurations, the general idea would still apply. In any case, as demonstrated in Section V, a path towards extracting the complex permittivity and thickness of dielectrics from *passive* sensor data exists even if the objective functions require modifications. For practical implementation, the technique described above requires knowledge of the following (i) physical temperatures of all layers and (ii) material properties of clothing and skin. In security sensing, the physical temperatures of all layers may be assumed to be equal to human body temperature [18]. Therefore, apart from natural variations, assuming average human body temperature measurement may yield acceptable results. Alternatively, approaches to measure human body temperature in real-time such as adding an additional radiometric band or an IR sensor to measure the temperature of uncovered skin may be considered. The former approach will require modifications to the objective functions to enable extraction of the physical temperature along with complex permittivity and thickness. The complex permittivity of skin along with its variation and impact on accuracy will be known parameters and characterized prior to deployment of the sensor. A database of the material properties of common clothing will need to be created. Alternatively, further study may be conducted to expand the use of *pactive* data to extract the properties of both clothing and the unknown layer.

From a sensor design standpoint, antenna research to obtain very high lateral resolution is critical since the extraction technique applies to a single voxel and assumes planar dielectrics. The planar dielectric assumption may hold true if the size of the measurement voxel is small. For lateral voxel resolution of the order of a few millimeters, it may be more appropriate to design the sensor in the W-band or higher frequencies to ensure compact antenna or array

sizes. Integration of the passive and active subsystems with potential reuse of antenna and front-end amplifiers would be appropriate. Additionally, the radar and radiometer cannot operate at the same time since the radar signal might damage the radiometric detector unless they operate in different frequency bands.

VII. CONCLUSION

This work examines the feasibility of extracting the dielectric constant, loss tangent and thickness of planar concealed items using a combination of passive and active (*pactive*) data with a focus on potential security applications. Crucially, the presented technique works even for normal incidence angles which suits security applications very well. For proof-of-concept demonstrations in this work, the data are acquired using independent K-band FMCW radar and total power radiometer. The technique comprises of optimizing three (active) radar-based objective functions and the (passive) radiometric error. The radar-based functions are used to calculate thickness and dielectric constant, following which the loss tangent is calculated using the radiometric objective function. Accurate extraction of all three parameters, especially the loss tangent, is challenging using band-limited active data alone. However, in thermodynamic equilibrium, the emissivity of any material is equal to the absorptivity [3]. Therefore, brightness temperature measured by the passive sensor provides information on the loss tangent.

When one material property like the thickness is known, the proposed technique yields accurate results for the dielectric constant and loss tangent of the unknown layer, as demonstrated using simulations. When none of the properties of the layer are known, the technique results in a solution that lies in the vicinity of the actual solution. Making two radiometric measurements, e.g., at different frequencies,
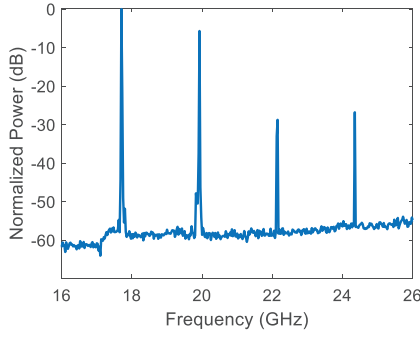
FIGURE A.I. Radar spectrum measured using spectrum analyzer for a single tone input.

can potentially improve the accuracy of the extraction process especially in the presence of measurement noise. The technique is validated experimentally with planar dielectrics (LDPE, AD450 and air) stacked on top of warm water, which is used as a simplified human body phantom. The goal is to extract the properties of the embedded AD450 layer under the assumption that all other layers are well known. A two-step optimization process consisting of a coarse optimization to find a narrow range of values for all three parameters of interest followed by a fine optimization using a different radiometric data point yielded less than 5% error in all extracted parameters. Therefore, this work demonstrates that *pactive* sensing is suitable for the characterization of embedded dielectric layers particularly at normal incidence angles of measurement. While the focus herein is security sensing, the technique may be applied to other dielectric characterization applications such as food processing, biological applications such as measuring water content in infiltrated fat, buried forest fires, drug delivery, characterization of laminated materials, etc. wherein more than one property of the embedded layer is unknown.

APPENDIX

The signal $S_{TX}^{radar}(t)$ transmitted by a frequency modulated continuous wave radar as a function of time t may be expressed as

$$S_{TX}^{radar}(t) = |S_{TX}(t)| \cos\left(2\pi t\left(f_0^{rad} + \frac{Wt}{2}\right) + 2\pi\theta_{TX}(t)\right) \quad \text{(A.1)}$$

where, $|S_{TX}|$ is the magnitude of the transmitted signal and may consist of amplitude distortions introduced by the transmitter, f_0^{rad} is the minimum frequency of the radar, W is the chirp rate, and $\theta_{TX}(t)$ is the phase distortion introduced by the transmitter. This signal reflects off the target and returns to the radar after a flight time of T_p. The received signal is expressed as

$$R_{TX}^{radar}(t) = \rho(f).|S_{TX}(t - T_p)| \cos\left(2\pi(t - T_p)\right. $$
$$\left. - \left(f_0^{rad} + \frac{W(t - T_p)}{2}\right) + 2\pi\theta_{TX}(t - T_p)\right) \quad \text{(A.2)}$$

where, ρ is the reflection coefficient of the target which is a function of frequency. This signal is mixed with the transmitted signal and filtered to yield an intermediate signal represented in the complex analytic equivalent form as

$$a_{IF}(t) = |S_{IF}|E(t)\rho(f)exp\big(j(2\pi WT_p + 2\pi\theta(t))\big) \quad \text{(A.3)}$$

where, $|S_{IF}|$ is an amplitude scaling during the mixing process. $E(t)$ and $\theta(t)$ represent the net amplitude distortion, respectively. Hence, the calibration in Eq. (1) extracts a signal that is proportional to $\rho(f) \exp(j2\pi WT_p)$ containing both information about reflection coefficient as well as distance.

A single frequency tone was input to the prototype radar instead of the sweeping VCO and its output is recorded using a spectrum analyzer in Fig. A.I. Instead of a single output tone, multiple peaks are observed indicating that the multiplier circuity is not filtering the harmonics sufficiently. For a sweeping input, the output should appear as multiple overlapping chirp signals. Hence, the following modifications are made

$$S_{TX}^{radar}(t) = \sum_{i=1}^{N} |S_{TX,i}(t)|cos\left(2\pi jt\left(f_{0,i}^{rad} + \frac{W_it}{2}\right)\right.$$
$$\left. + 2\pi j\theta_{TX,i}(t)\right) \quad \text{(A.4)}$$

$$R_{TX}^{radar}(t) = \sum_{i=1}^{N} \rho_i(f)|S_{TX,i}(t - T_p)| \cos\left(2\pi j(t - T_p)\right.$$
$$\left. - \left(f_{0,i}^{rad} + \frac{W_i(t - T_p)}{2}\right) + 2\pi j\theta_{TX,i}(t - T_p)\right) \quad \text{(A.5)}$$

The intermediate signal is obtained by mixing the above two signals and passing through a low pass filter, i.e., selecting the subtractive terms. The complex analytic equivalent as in (A.3) is then calculated using the Hilbert transform. For highly reflective targets when $|\rho(f)| = 1$ the calibration process of dividing the signal by that from a metal plate extracts the distance as demonstrated experimentally in [21] for a scene containing more than one target. However, the efficacy of the calibration process decreases due to the excess terms present in (A.4) - (A.5) when compared to (A.1)–(A.2). The reflection coefficient of the target $\rho_i(f)$ shows strong frequency dependencies (see Fig. 11) that are absent in the metallic calibration target. From (A.3), in the absence of the harmonics, the calibration process will be able to extract a quantity that is proportional to the reflection coefficient. However, dividing the series in (A.5) with another series for the metal does not yield the reflection coefficient. Hence, the performance should improve if the harmonics are properly filtered.

REFERENCES

[1] J. A. Nanzer, *Microwave and Millimeter-Wave Remote Sensing for Security Applications*. Boston, MA, USA: Artech House, 2012.

[2] A. Dallinger, S. Schelkshorn, and J. Detlefsen, "Short distance related security millimeter-wave imaging systems," in *Proc. German Microw. Conf. (GeMIC)*, 2005, pp. 244–246.

[3] F. T. Ulaby, R. K. Moore, and A. K. Fung, *Microwave Remote Sensing: Active and Passive. Volume 1-Microwave Remote Sensing Fundamentals and Radiometry*. Norwood, MA, USA: Artech House, 1981.

[4] D. M. Sheen, D. L. McMakin, and T. E. Hall, "Three-dimensional millimeter-wave imaging for concealed weapon detection," *IEEE Trans. Microw. Theory Techn.*, vol. 49, no. 9, pp. 1581–1592, Sep. 2001, doi: 10.1109/22.942570.

[5] D. M. Sheen, D. L. McMakin, T. E. Hall, and R. H. Severtsen, "Active millimeter-wave standoff and portal imaging techniques for personnel screening," in *Proc. IEEE Conf. Technol. Homeland Security*, May 2009, pp. 440–447, doi: 10.1109/THS.2009.5168070.

[6] T. D. Williams and N. M. Vaidya, "A compact, low-cost, passive MMW security scanner," in *Proc. Passive Millimeter-Wave Imag. Technol. VIII*, 2005, pp. 109–117.

[7] W. J. D. Johnson, T. Weller, and X. Gong, "Pactive sensors for security applications," in *Proc. WAMICON*, Apr. 2013, pp. 1–4, doi: 10.1109/WAMICON.2013.6572781.

[8] "Concealed objects stand-off real-time imaging for security." European Commission. Accessed: Nov. 17, 2022. [Online]. Available: https://cordis.europa.eu/project/id/312745

[9] R. K. Moore and F. T. Ulaby, "The radar radiometer," *Proc. IEEE*, vol. 57, no. 4, pp. 587–590, Apr. 1969.

[10] L. Hai, X. Miaoxin, W. Chong, H. Yaokui, and Z. Shouxiang, "Ground-based remote sensing of LWC in cloud and rainfall by a combined dual-wavelength radar-radiometer system," *Adv. Atmosp. Sci.*, vol. 2, no. 1, pp. 93–103, 1985.

[11] R. Meneghini, H. Kumagai, J. R. Wang, T. Iguchi, and T. Kozu, "Microphysical retrievals over stratiform rain using measurements from an airborne dual-wavelength radar-radiometer," *IEEE Trans. Geosci. Remote Sens.*, vol. 35, no. 3, pp. 487–506, May 1997, doi: 10.1109/36.581956.

[12] A. V. Kouraev et al., "Synergy of active and passive satellite microwave data for the study of first-year sea ice in the Caspian and Aral seas," *IEEE Trans. Geosci. Remote Sens.*, vol. 42, no. 10, pp. 2170–2176, Oct. 2004, doi: 10.1109/TGRS.2004.835307.

[13] W. H. Peake, R. L. Riegler, and C. H. Schultz, "The mutual interpretation of active and passive microwave sensor outputs(Interdependent microwave radar- and radiometer- sensor measurements of backscatter and albedo characteristics of earth surface)," Patent NASA-CR-77 987, 1966.

[14] D. G. Macfarlane et al., "Passive and active imaging at 94 GHz for environmental remote sensing," in *Proc. Passive Active Millimeter-Wave Imag. XVI*, 2013, Art. no. 87150L.

[15] D. Entekhabi et al., "The soil moisture active passive (SMAP) mission," *Proc. IEEE*, vol. 98, no. 5, pp. 704–716, May 2010.

[16] D. A. Robertson et al., "High resolution, wide field of view, real time 340GHz 3D imaging radar for security screening," in *Proc. Passive Active Millimeter-Wave Imag. XX*, 2017, Art. no. 101890C.

[17] J. Hassel et al., "Dual-band submillimeter-wave kinetic inductance bolometers and an imaging system for contraband object detection," in *Proc. Passive Active Millimeter-Wave Imag. XXI*, 2018, Art. no. 106340F.

[18] R. Appleby, H. Petersson, and S. Ferguson, "Concealed object stand-off real-time imaging for security: CONSORTIS," in *Proc. Passive Active Millimeter-Wave Imag. XVIII*, 2015, Art. no. 946204.

[19] D. K. Ghodgaonkar, V. V. Varadan, and V. K. Varadan, "Free-space measurement of complex permittivity and complex permeability of magnetic materials at microwave frequencies," *IEEE Trans. Instrum. Meas.*, vol. 39, pp. 387–394, 1990, doi: 10.1109/19.52520.

[20] *N1500A Materials Measurement Suite*, Keysight Technol., Santa Rosa, CA, USA, 2018, pp. 5–14.

[21] J. Baker-Jarvis, E. J. Vanzura, and W. A. Kissick, "Improved technique for determining complex permittivity with the transmission/reflection method," *IEEE Trans. Microw. Theory Techn.*, vol. 38, no. 8, pp. 1096–1103, Aug. 1990, doi: 10.1109/22.57336.

[22] A. Kocakusak and S. Helhel, "Marble pre-selection chart to suppress EMF in S-band and SAR reduction capabilities of them at 2.45 GHz," *IETE J. Res.*, to be published, doi: 10.1080/03772063.2021.1972846.

[23] S. Helhel, A. Kocakusak, and M. Sunel, "Determining loss tangent values of dry granite for potential S-band applications," *Microw. Opt. Technol. Lett.*, vol. 62, no. 11, pp. 3476–3484, 2020.

[24] J. Baker-Jarvis, M. D. Janezic, and D. C. Degroot, "High-frequency dielectric measurements," *IEEE Instrum. Meas. Mag.*, vol. 13, no. 2, pp. 24–31, Apr. 2010, doi: 10.1109/MIM.2010.5438334.

[25] G. Brodie, M. V. Jacob, and P. Farrell, "6 techniques for measuring dielectric properties," in *Microwave and Radio-Frequency Technologies in Agriculture*. Warsaw, Poland: De Gruyter Open Poland, 2015, pp. 52–77.

[26] Z. Akhter and M. J. Akhtar, "Time domain microwave technique for dielectric imaging of multi-layered media," *J. Electromagn. Waves Appl.*, vol. 29, no. 3, pp. 386–401, Feb. 2015, doi: 10.1080/09205071.2014.997840.

[27] I. Alawneh, J. Barowski, and I. Rolfes, "Measuring the permittivity of dielectric materials by using 140 GHz FMCW radar sensor," in *Proc. 13th Eur. Conf. Antennas Propag. (EuCAP)*, Mar./Apr. 2019, pp. 1–4.

[28] J. Barowski and I. Rolfes, "Millimeter wave material characterization using FMCW-transceivers," in *Proc. IEEE MTT-S Int. Microw. Workshop Ser. Adv. Mater. Process. RF THz Appl. (IMWS-AMP)*, Sep. 2017, pp. 1–3, doi: 10.1109/IMWS-AMP.2017.8247432.

[29] A. N. Nguyen and H. Shirai, "A free space permittivity measurement at microwave frequencies for solid materials," *IEICE Trans. Electron.*, vol. 100, no. 1, pp. 52–59, 2017.

[30] A. Schiessl and S. S. Ahmed, "W-band imaging of explosive substances," in *Proc. Eur. Microw. Conf. (EuMC)*, Sep./Oct. 2009, pp. 1888–1891, doi: 10.23919/EUMC.2009.5296150.

[31] J. L. Frolik and A. E. Yagle, "Forward and inverse scattering for discrete layered lossy and absorbing media," *IEEE Trans. Circuits Syst. II, Analog Digit. Signal Process.*, vol. 44, no. 9, pp. 710–722, Sep. 1997, doi: 10.1109/82.624998.

[32] J. L. Frolik and A. E. Yagle, "Reconstruction of multilayered lossy dielectrics from plane wave impulse responses at two angles of incidence," *IEEE Trans. Geosci. Remote Sens.*, vol. 33, no. 2, pp. 268–279, Mar. 1995, doi: 10.1109/TGRS.1995.8746008.

[33] J. Frolik, "Reconstruction of multilayered lossy dielectrics from one-sided plane wave impulse reflection responses: The bistatic case," *IEEE Trans. Geosci. Remote Sens.*, vol. 39, no. 9, pp. 2051–2059, Sep. 2001, doi: 10.1109/36.951095.

[34] O. B. McMahon, E. R. Brown, G. D. Daniels, T. J. Murphy, and G. L. Hover, "Oil thickness detection using wideband radiometry," in *Proc. Int. Oil Spill Conf.*, 1995, pp. 15–19, 1995, doi: 10.7901/2169-3358-1995-1-15.

[35] J. Lemmetyinen et al., "Snow density and ground permittivity retrieved from L-band radiometry: Application to experimental data," *Remote Sens. Environ.*, vol. 180, pp. 377–391, Jul. 2016. [Online]. Available: https://doi.org/10.1016/j.rse.2016.02.002

[36] A. Menon, G. Mumcu, and T. M. Weller, "Implementation and enhancement of Hilbert transform-based calibration in a K band FMCW radar for high-resolution security applications," in *Proc. Radar Sens. Technol. XXII*, 2018, Art. no. 106330N.

[37] K. B. Cooper, R. J. Dengler, N. Llombart, B. Thomas, G. Chattopadhyay, and P. H. Siegel, "THz imaging radar for standoff personnel screening," *IEEE Trans. THz Sci. Technol.*, vol. 1, no. 1, pp. 169–182, Sep. 2011, doi: 10.1109/TTHZ.2011.2159556.

[38] A. Menon, A. Snider, G. Mumcu, and T. Weller, "An 18–26 GHz range calibrated linear synthetic aperture radar prototype suitable for security applications," in *Proc. IEEE 19th Wireless Microw. Technol. Conf. (WAMICON)*, Apr. 2018, pp. 1–4, doi: 10.1109/WAMICON.2018.8363894.

[39] A. Menon, M. D. Grady, and T. Weller, "A generalized radiometer system equation that includes temperature-dependent system losses," in *Proc. IEEE 20th Wireless Microw. Technol. Conf. (WAMICON)*, Apr. 2019, pp. 1–4, doi: 10.1109/WAMICON.2019.8765473.

[40] J. P. Randa and L. Terrell, "Noise-temperature measurement system for the WR-28 band," Technical Note (NIST TN)-1395, NIST, Gaithersburg, MD, USA, 1997.

[41] A. Menon and T. M. Weller, "A novel background calibration technique for microwave radiometric sensors in indoor applications," *IEEE Sens. Lett.*, vol. 4, no. 12, pp. 1–4, Dec. 2020, doi: 10.1109/LSENS.2020.3042776.

[42] T. T. Wilheit, "Radiative transfer in a plane stratified dielectric," *IEEE Trans. Geosci. Electron.*, vol. GE-16, no. 2, pp. 138–143, Apr. 1978, doi: 10.1109/TGE.1978.294577.

[43] R. E. Collin, *Field Theory of Guided Waves*. New York, NY, USA: Wiley, 1990.

[44] G. L. Charvat, "A low-power radar imaging system," M.S. thesis, Dept. Electr. Comput. Eng., Michigan State Univ., East Lansing, MI, USA, 2007.

[45] "PTFE/woven fiberglass/ceramic filled laminate for microwave printed circuit boards," Data Sheet Arlon AD450, Arlon Microw. Mater., Rancho Cucamonga, CA, USA. Accessed: Nov. 17, 2022. [Online]. Available: https://elcopcbonline.com/custom/materials/ARLON/AD450.pdf

[46] M. Kacar, T. M. Weller, and G. Mumcu, "3D printed wideband multilayered dual-polarized stacked patch antenna with integrated MMIC switch," *IEEE Open J. Antennas Propag.*, vol. 2, pp. 38–48, 2021, doi: 10.1109/OJAP.2020.3041959.

[47] D. J. Daniels, *EM Detection of Concealed Targets*. Hoboken, NJ, UA: Wiley, 2009.

[48] U. Kaatze, "Complex permittivity of water as a function of frequency and temperature," *J. Chem. Eng. Data*, vol. 34, no. 4, pp. 371–374, 1989.

[49] C. Balamati and R. Jha, *Soft Computing in Electromagnetics: Methods and Applications*. Cambridge, U.K.: Cambridge Univ. Press, 2016.

[50] S. I. Alekseev and M. Ziskin, "Human skin permittivity determined by millimeter wave reflection measurements," *Bioelectromagn. J. Bioelectromagn. Soc. Soc. Phys. Regul. Biol. Med. Eur. Bioelectromagn. Assoc.*, vol. 28, no. 5, pp. 331–339, 2007.

[51] R. Salvado, C. Loss, R. Gonçalves, and P. Pinho, "Textile materials for the design of wearable antennas: A survey," *Sensors*, vol. 12, no. 11, pp. 15841–15857, 2012.

ARYA MENON (Member, IEEE) received the Bachelor of Engineering degree in electronics and communication from the Manipal Institute of Technology, Manipal, India, in 2014, the M.S. degree in electrical engineering from the University of South Florida in 2016, and the Ph.D. degree in electrical and computer engineering from Oregon State University in 2021. She is currently a Postdoctoral Fellow with Texas A&M University. Her research interests include radars, radiometers, sensor calibration techniques, and hardware-software codesign techniques for AI in electromagnetic sensors. Her research has earned multiple awards, including selection as a 2022 DARPA Riser, the 2020 ARTFG Roger Pollard Student Fellowship, and the 2019 IEEE Microwave Theory and Techniques Society Graduate Fellowship.

THOMAS M. WELLER (Fellow, IEEE) received the Ph.D. degree in electrical engineering from the University of Michigan in 1995. He joined Oregon State University in 2018, as a Professor and the Head of the School of Electrical Engineering and Computer Science. He was a Faculty Member with the University of South Florida from 1995 to 2018. He co-founded Modelithics in 2001. His research focuses on microwave circuits, sensors and antennas, including an emphasis on the use of additive manufacturing. He has published over 300 journal and conference papers and three book chapters, holds over 40 U.S. patents. He is a Fellow the National Academy of Inventors.